INORGANIC CHEMISTRY FRONTIERS

RESEARCH ARTICLE

View Article Online
View Journal | View Issue

Cite this: *Inorg. Chem. Front.*, 2026, **13**, 628

A monolithic chiral perovskite crystal enables self-powered, full-Stokes detection of ultra-weak light

Quanlin Chen, *[a] Yangbin Xu,[a] Qingming Wu,[a] Yanxing Feng,[b] Zhiqiang Huang, [a] Hai Jia, [c] Shaoming Ying*[a] and Xiaohui Huang *[a]

Accurate and chip-integrated full-Stokes polarization detection is essential for advancing multifunctional optoelectronic systems. However, conventional approaches relying on optical filters often suffer from significant optical losses and poor sensitivity under weak-light conditions. Here, we report an efficient full-Stokes polarimeter based on a 1D chiral-polar perovskite, (*R*/*S*-NEA)PbI_3. The intrinsic anisotropic and chiral structure of the (*R*/*S*-NEA)PbI_3 single crystal enables both high linear and circular polarization sensitivity. Moreover, the polar structure induces a giant bulk photovoltaic effect (BPVE) of up to 8 V, enabling efficient carrier extraction under zero bias and significantly suppressing noise currents to the ~fA level, resulting in an exceptional specific detectivity of 4.1 × 10^{13} Jones. These combined properties enable accurate, self-powered full-Stokes polarization detection, with the fabricated single-crystal-based polarimeter achieving an average Stokes parameter error (ΔS_{1-3}) of less than 3%. Notably, the polarimeter demonstrates an ultra-low detection limit of 0.4 μW cm^{-2}, representing the highest sensitivity among comparable polarimeters reported to date. With easy on-chip integration, the polarimeter showcases precise full-Stokes imaging capabilities.

Received 24th September 2025,
Accepted 28th October 2025

DOI: 10.1039/d5qi01944c

rsc.li/frontiers-inorganic

Introduction

The state of polarization (SoP), which describes the oscillation direction of the electric field, is a fundamental parameter in optics, playing a critical role in diverse applications such as quantum optics, remote sensing, and astronomy.[1–4] Current state-of-the-art SoP detection technologies rely on full-Stokes polarimeters that integrate metasurfaces or diffraction gratings. However, these components often introduce significant optical losses and fabrication complexity, which in turn limit the detection sensitivity—particularly under low-light conditions—thereby restricting their practical applicability in weak-light polarization sensing.

An ideal approach to overcoming these challenges is to develop semiconducting materials with intrinsic polarization sensitivity. Among the candidates, hybrid metal–halide perovskites stand out due to their outstanding optoelectronic properties and rich chemical tunability.[5–9] For instance, dimensional engineering can induce anisotropic lattice structures, while the incorporation of chiral organic ligands can transfer chirality to the inorganic framework, enabling selective responses to both linearly polarized light (LPL) and circularly polarized light (CPL).[10,11] These structural features endow perovskites with inherent polarization sensitivity. Moreover, the tunable polar structures of perovskites offer another promising pathway to realize ultra-sensitive full-Stokes polarimetry. By breaking inversion symmetry—achievable through specific polar point groups—perovskites can exhibit bulk photovoltaic effects (BPVEs),[12,13] which allows polarimeters to operate under zero-bias conditions with minimal noise current, while enhancing polarization sensitivity under low-light illumination.

Recent progress has demonstrated the feasibility of using chiral perovskites for full-Stokes photodetection. While high-performance SoP polarimeters have been realized using patterned 2D and 3D chiral perovskites with aligned nanowires,[14–19] the complex and costly fabrication processes involved present significant drawbacks. Consequently, a more streamlined approach of integrating anisotropy and chirality directly into the perovskite crystal lattice has become a promising strategy for high-performance detection.[20–22] Despite this progress, a fundamental limitation persists. Most intrinsically

[a]*College of New Energy and Materials, Ningde Normal University, Key Laboratory of Featured Materials in Biochemical Industry, Ningde 352100, P. R. China. E-mail: siqichen123@hotmail.com, 11429721@qq.com, yingshaoming@126.com*
[b]*Institute of Advanced Ceramics, Henan Academy of Sciences, Zhengzhou, 450046, P. R. China*
[c]*College of Mathematics and Physics, Ningde Normal University, Ningde 352100, China*

polarization-sensitive perovskites are plagued by large noise currents, which restrict their detection capabilities to optical intensities above the microwatt-per-square-centimeter (μW cm^{-2}) threshold. This limitation poses a significant barrier for applications requiring the detection of weak signals or subtle polarization variations, highlighting the urgent need for more promising materials.

In this work, we report 1D chiral-polar (*R*/*S*-NEA)PbI_3 (*R*-NEA = *R*-(+)-1-(1-naphthyl)ethylamine, *S*-NEA = *S*-(−)-1-(1-naphthyl)ethylamine) that exhibits a big BPVE of up to 8 V. This intrinsic BPVE enables efficient carrier extraction under zero bias and suppresses noise currents to the ~fA level, yielding a high specific detectivity of 4.1×10^{13} Jones. The intrinsic anisotropic and chiral structure of (*R*/*S*-NEA)PbI_3 enables high linear polarization sensitivity, with a polarization ratio (ω) of 1.99 and a robust CPL anisotropic factor (g_{cpl}) of 0.57. These combined properties enable accurate, self-powered full-Stokes polarization detection, with the fabricated single-crystal-based polarimeter achieving an average Stokes parameter error (ΔS_{1-3}) of less than 3%. Remarkably, the polarimeter achieves an ultra-low detection limit of 0.4 μW cm^{-2}, representing the highest sensitivity reported to date among comparable systems. Benefiting from facile on-chip integration, the polarimeter further enables precise full-Stokes polarization imaging.

Results and discussion

We use temperature-cooling methods to grow the centimeter-sized (*R*/*S*-NEA)PbI_3 single crystal (SC), as shown in Fig. S1. The crystallographic structure presents that the chiral NEA^+ cations surround face-sharing $[PbI_6]^{4-}$ octahedral chains *via* hydrogen bonding (Fig. 1a). This interaction induces chirality transfer from the organic cations to the inorganic framework, forming helically arranged $[PbI_6]^{4-}$ chains along the *a*-axis—a structural motif that promotes strong light–matter interactions with CPL. Moreover, these $[PbI_6]^{4-}$ chains exhibit anisotropic topological arrangement along intrachain (*a*-axis) and out-of-chain (*b*- or *c*-axis) directions, thereby imparting structural features favorable for LPL detection (Fig. 1b).

Notably, (*R*/*S*-NEA)PbI_3 breaks the structural inversion symmetry into a special polar characteristic. Grazing-incidence wide-angle X-ray scattering (GIWAXS) measurements of (*R*-NEA)PbI_3 reveal distinct (010) and (012) diffraction peaks belonging to the C_2 space group (Fig. 1c). This observation aligns with prior studies and confirms that the synthesized crystals belong to one of the 16 chiral polar point groups—non-centrosymmetric groups that possess nonzero gyration tensors in the helical $[PbI_6]^{4-}$ chain direction (as shown in Fig. 1d). The chiral-polar structure is expected to facilitate the

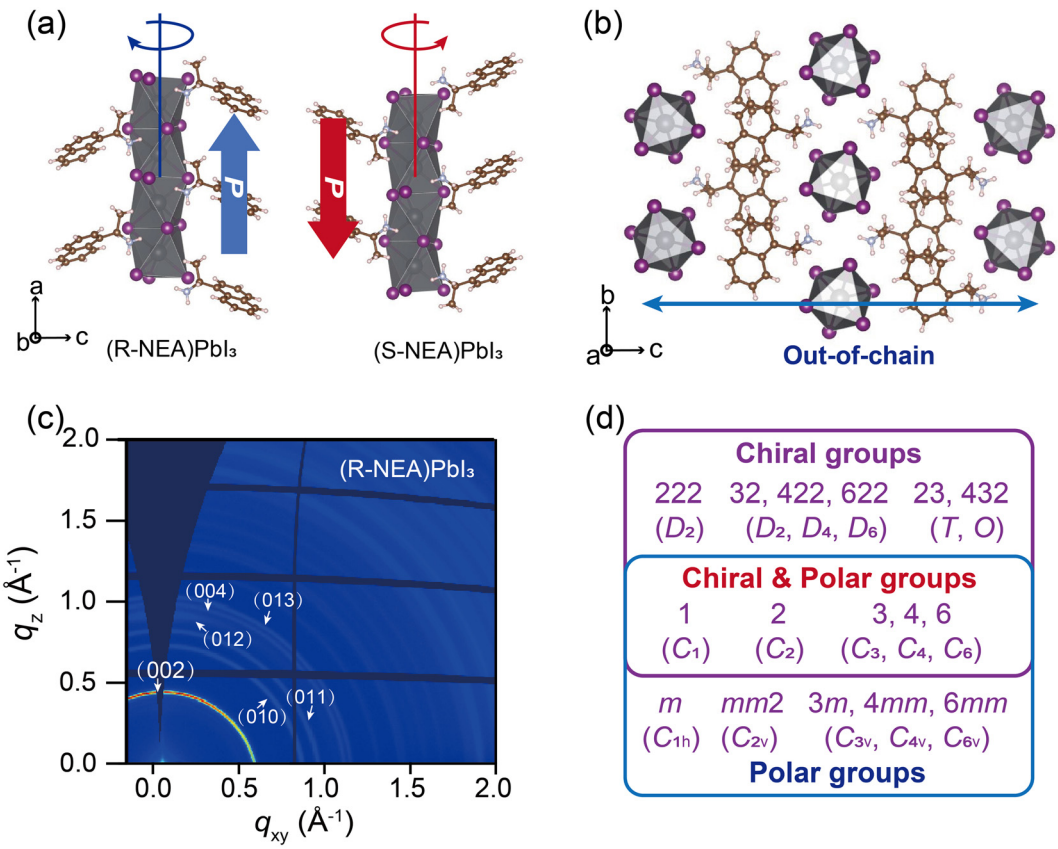

Fig. 1 The schematic illustration of (*R*-NEA)PbI_3 and (*S*-NEA)PbI_3: (a) chiral and polar crystallographic structures; (b) anisotropic crystallographic structure. (c) GIWAX pattern of the (*R*-NEA)PbI_3 SC powder. (d) Possible second-rank axial tensor forms for 16 non-centrosymmetric space groups with chiral and polar characteristics, among which only five exhibit both chiral and polar properties.

BPVE, which enables spontaneous photocarrier separation and extraction under zero bias—an essential mechanism for enhancing polarization sensitivity under weak-light conditions.[23,24]

We perform azimuth-dependent reflectance difference microscopy (ADRDM) to quantitatively investigate the anisotropic optical properties of (*R*/*S*-NEA)PbI_3 SC. This technique assesses the normalized reflectance difference ($\Delta R/R$) along two orthogonal in-plane directions under linearly polarized light. For (*R*/*S*-NEA)PbI_3 SCs with arbitrary in-plane orientations, the angular dependence of $\Delta R/R(\theta)$ can be modeled as follows:[25]

$$\Delta R/R(\theta) = \Delta R/R_{ab} \cos 2(\theta - \theta_0) \quad (1)$$

Here, $\Delta R/R_{ab}$ is calculated as $\Delta R/R_{ab} = 2(R_a - R_b)/(R_a + R_b)$, where R_a and R_b denote the reflectance along the *a*-axis and the *b*-axis, respectively. θ is the azimuthal angle of the incident polarization relative to the lab frame, and θ_0 is the angle between the *a*-axis of the crystal and the initial reference direction. Fig. 2a displays the optical image of the (*R*-NEA)PbI_3 crystal measured by ADRDM, with a black Cartesian coordinate system indicating the azimuthal angle θ. In the initial measurement, the polarization direction of the incident light is aligned with the *a*-axis of the crystal. During image recording, the angle is rotated counterclockwise in 15° increments. ADRDM images at angles varying from 0° to 180° reveal significant brightness variations across the surface of the (*R*-NEA)PbI_3 SC (Fig. 2b). The $\Delta R/R$ values extracted from each ADRDM image exhibit a clear sinusoidal trend, as shown in Fig. 2c. Notably, $\Delta R/R$ reaches a maximum of 0.16 and a minimum of −0.15 at azimuthal angles of approximately 180° and 90°, corresponding closely to the crystallographic *a*- and *b*-axis directions, respectively.

To gain deeper insight into the anisotropic light–matter interactions, we performed angle-resolved polarized Raman spectroscopy on the crystal's *ab*-plane. The resulting spectra, shown in Fig. S2a and b, distinctly reveal that the Raman intensity is strongly dependent on the polarization angle of the incident laser. In particular, the prominent low-frequency mode at 53 cm^{-1}, which is attributed to the stretching vibration of the $[PbI_6]^{4-}$ octahedra, is analyzed. As plotted in the inset of Fig. S2b, the intensity of this mode follows a clear sinusoidal pattern as a function of polarization angle. This periodic variation is a direct signature of an anisotropic vibrational mode, confirming that the crystal lattice exhibits an asymmetric response to LPL along the *a*- and *b*-axes.

The chiroptical properties of the material are further characterized using circular dichroism (CD) spectroscopy. To eliminate interference from linear birefringence (LB) and linear dichroism (LD), we measure CD signals from both the front and back sides of the crystal and apply calibration based on established protocols.[26] As shown in Fig. 2d, (*R*-NEA)PbI_3 and (*S*-NEA)PbI_3 exhibit strong and opposite CD signals

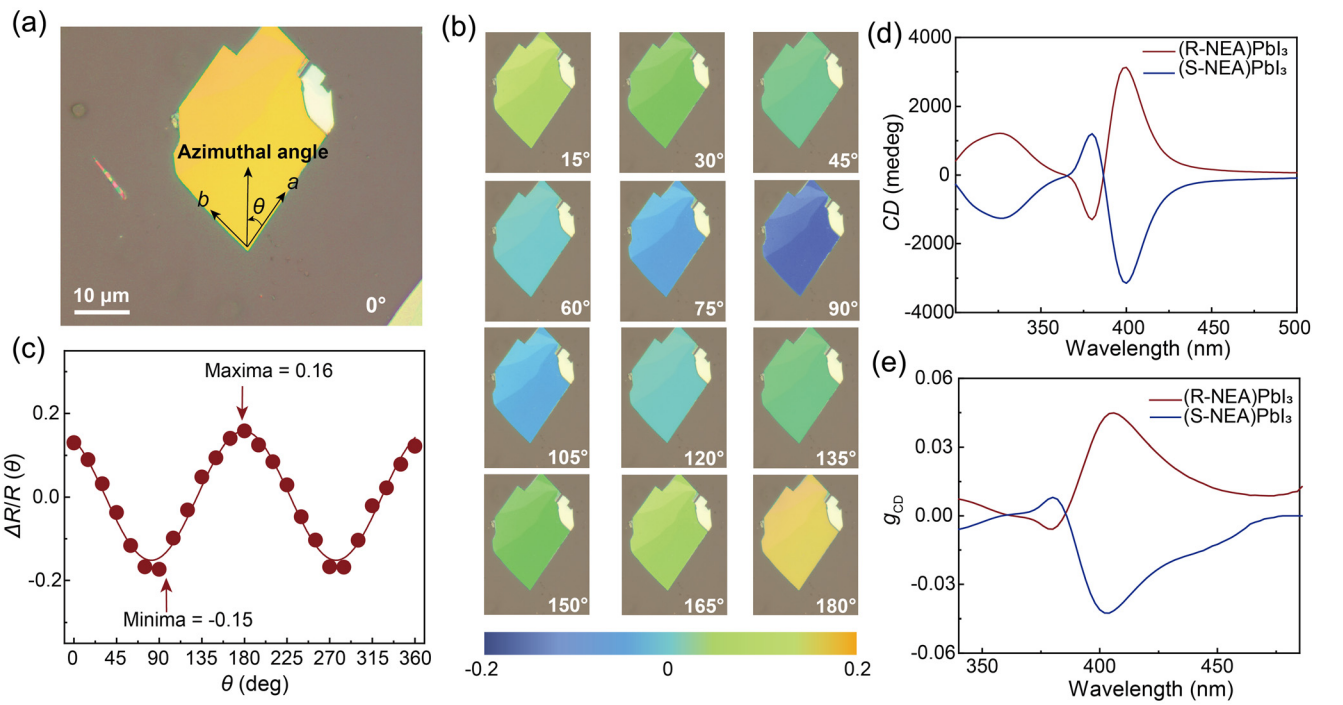

Fig. 2 (a) Optical image of (*R*-NEA)PbI_3 SC on a silicon substrate. The black Cartesian coordinate frame defined along the *a*- and *b*-axes is used as the reference for the azimuthal angle (θ). (b) ADRDM images acquired at azimuthal angles from 15° to 180°. (c) Polar plot of $\Delta R/R$ as a function of the azimuthal angle θ, extracted from the ADRDM images. (d) CD spectra of (*R*-/*S*-NEA)PbI_3 films. (e) Corresponding g_{CD} spectra of (*R*-/*S*-NEA)PbI_3 films.

near the exciton resonance (Fig. S3). The corresponding CD anisotropy factor (g_{CD}) extracted from the spectrum is estimated to be approximately 0.044 (Fig. 2e), which exceeds the values reported for previously studied chiral perovskites.[27–31] This suggests a strong intrinsic response to CPL-vector detection.

To investigate the photoelectronic properties of (*R*-NEA)PbI_3, we fabricated a lateral-configuration device, as illustrated in Fig. 3a. We first explored the BPVE in 1D (*R*-NEA)PbI_3 SC by measuring the photocurrent–voltage (*I*–*V*) characteristics along the *a*- and *b*-axis directions, which correspond to the intrachain and out-of-chain directions, respectively. As shown in Fig. 3b, a pronounced BPVE is observed along the *a*-axis, characterized by a short-circuit current of approximately 0.5 nA and an open-circuit voltage (V_{oc}) as high as 8 V. Critically, the magnitude of V_{oc} scaled linearly with increasing electrode distance (Fig. S4a and b), which points to a uniform electric field originating from the BPVE.[31] For comparison, almost no BPVE photocurrent is observed along the *b*-axis due to the centrosymmetric nature in the out-of-plane direction (Fig. 3b inset). Moreover, an opposite negative current signal is observed in the (*S*-NEA)PbI_3 SC device (Fig. 3c), confirming that the BPVE originates from the intrinsic chiral polar structure rather than measurement artifacts.[9,32–36] These results suggest the presence of a strong internal electric field along the intrachain direction, which is advantageous for efficient carrier separation and extraction.

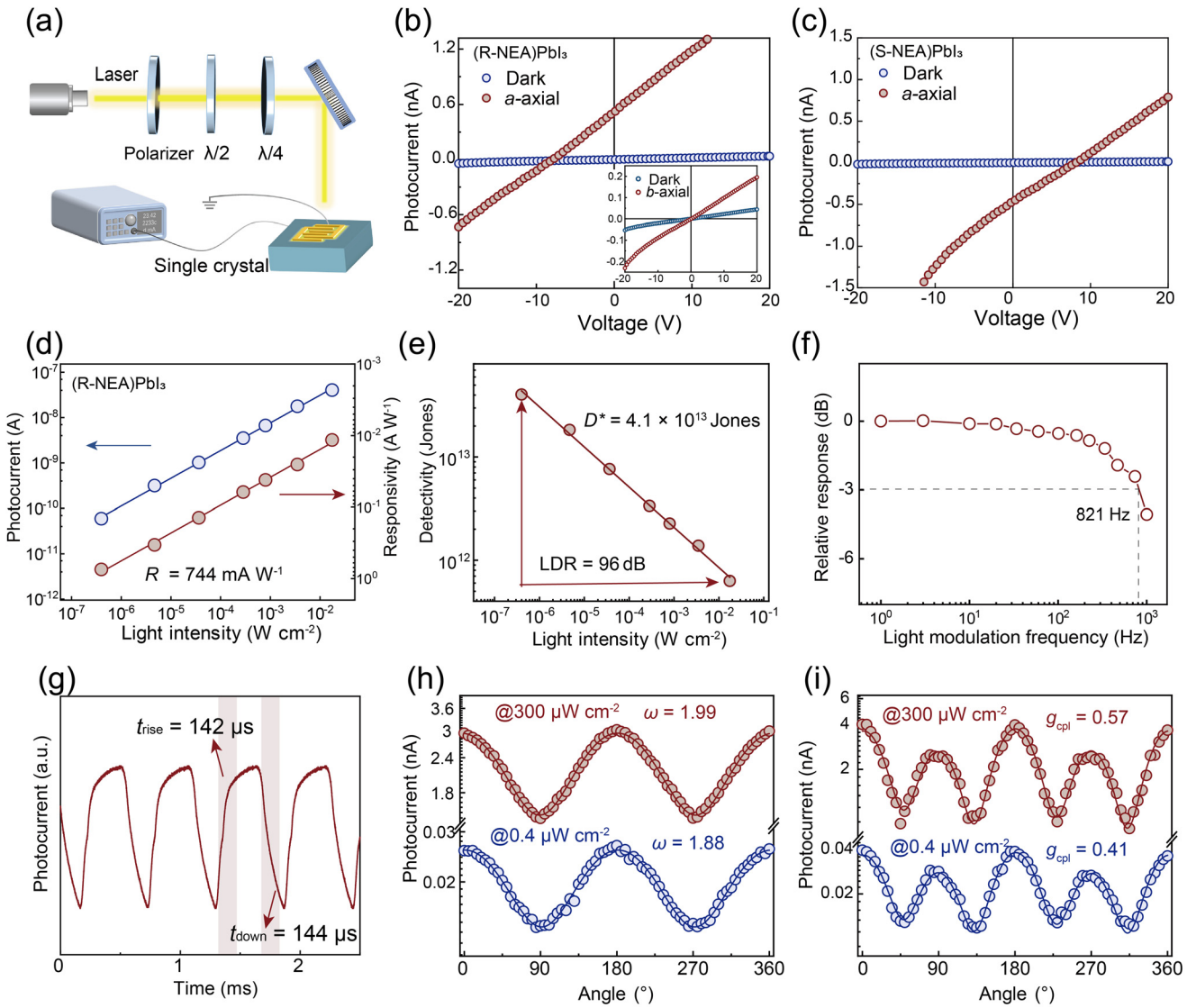

Fig. 3 (a) Schematic illustration of the experimental configuration for the polarization measurements; the polarization states are modulated using the $\lambda/2$ or $\lambda/4$ plates. Photocurrent *versus* voltage (*I*–*V*) measurements under 396 nm UV illumination: (b) electrodes assessed parallel to the *a*-axis and *b*-axis (inset) of (*R*-NEA)PbI_3 SC; (c) electrodes assessed parallel to the *a*-axis of (*S*-NEA)PbI_3 SC. (d) Photocurrent and responsivity of the (*R*-NEA)PbI_3 SC polarimeter measured under various light irradiation intensities at zero bias; and (e) corresponding detectivity extracted from responsivity. (f) Frequency photocurrent responses. (g) On–off photocurrent measurements. (h) LPL-dependent and (i) CPL-dependent photocurrent measurements under 396 nm illumination with intensities of 0.4 μW cm^{-2} and 300 μW cm^{-2}.

Encouraged by the strong BPVE, we fabricate a self-powered polarimeter by depositing lateral electrodes along the *a*-axis of (*R*-NEA)PbI_3. The photoresponse is characterized under 396 nm irradiation at various light intensities. The polarimeter exhibits a broad linear dynamic range (LDR) of 96 dB (Fig. 3d), with a calculated responsivity (R) of 744 mA W^{-1} and a corresponding External Quantum Efficiency (EQE) of 233% (Fig. S5). Due to the BPVE-driven carrier extraction, the polarimeter operates without an external bias, significantly reducing dark current fluctuations.[33,37–41] Correspondingly, the equivalent noise current under zero bias is estimated to be as low as 2.4 fA Hz^{-1} (Fig. S6). Owing to its high responsivity and ultra-low noise, the specific detectivity (D^*) of the polarimeter is determined to be 4.1×10^{13} Jones (and Fig. 3e), surpassing that ($\sim 10^{12}$ Jones) of commercial silicon photodetectors. This high detectivity is especially beneficial for detecting weak polarization signals buried in noise. Frequency-dependent photocurrent analysis reveals a high response bandwidth of up to 821 Hz (Fig. 3f). Also, the polarimeter demonstrates a fast temporal response, with rise and fall times of 142 μs and 144 μs (Fig. 3g), indicating that the (*R*-NEA)PbI_3 SC-based polarimeter is capable of high-speed optical sensing. Taken together, the combination of low noise, high detectivity, and fast response makes this chiral perovskite-based polarimeter a highly promising candidate for efficient polarization-sensitive photodetectors.

We further investigated the polarization discrimination capabilities of the (*R*-NEA)PbI_3 SC polarimeter. First, to optimize the device for LPL detection, we systematically varied the lateral electrode distance and selected 50 μm as the optimal channel width for fabrication (Fig. S7a and b). Using this optimized configuration, the device was illuminated with 396 nm light whose polarization state was controlled using a linear polarizer, a half-wave ($\lambda/2$), and a quarter-wave ($\lambda/4$) plate. As shown in Fig. 3h and Fig. S8, the (*R*-NEA)PbI_3 polarimeter exhibits a distinct periodic modulation in photocurrent under zero bias across a wide range of illumination intensities from 0.4 μW cm^{-2} to 300 μW cm^{-2}. Specifically, the polarization ratio ($\omega = I_{max}/I_{min}$, where I_{max} and I_{min} represent the maximum and minimum photocurrent responses under different polarization angles) is calculated to be 1.99 under 300 μW cm^{-2} illumination. Remarkably, even at ultra-low illumination of 0.4 μW cm^{-2}, the polarization ratio remains at 1.89, indicating minimal performance degradation. This high LPL discrimination surpasses that of most previously reported perovskite polarimeters.[40–42] The helical arrangement of the 1D inorganic framework generates a strong electric field, along with anisotropic absorbance in both intrachain and out-of-chain directions, which excludes the excellent polarization-sensitive performance.

Next, we assess the capability of (*R*-NEA)PbI_3 for CPL detection by analyzing the photocurrent difference under right-handed (RCP) and left-handed (LCP) circularly polarized illumination. Across the range of incident powers (0.4–300 μW cm^{-2}), the polarimeter demonstrates an almost consistent discrimination in photocurrent response between LCP and RCP (Fig. 3i and Fig. S9). By evaluating the photocurrent anisotropy factor (g_{cpl}) for CPL:

$$g_{cpl} = 2(I_L - I_R)/(I_L + I_R) \quad (2)$$

where I_L and I_R mean the photocurrent under LCP and RCP illumination, respectively. We obtain a g_{cpl} of 0.57 at 300 μW cm^{-2} and retain a high value of 0.41 even under weak illumination of 0.4 μW cm^{-2}. These results indicate that the robust BPVE in (*R*-NEA)PbI_3 enables efficient spin-dependent carrier extraction under zero bias, enabling reliable CPL discrimination even under ultra-weak light conditions.

We then explore the detection of the SoPs. Here, we use four Stokes parameters—total intensity S_0, two linear components S_1 and S_2, and the circular component S_3—to describe SoPs. Eight representative SoPs on the Poincaré sphere (modulated using $\lambda/2$ and $\lambda/4$ wave plates, as depicted in Fig. 4a) are inputted to evaluate detection accuracy. During the measurement process, the polarimeter is rotated at five angles (0°, 45°, 90°, 135°, and 180°) to record the photocurrent. As shown in Fig. 4b, the angle-dependent photocurrent fits well to sinusoidal functions and displays clear dependence on input polarization. By calibrating the photocurrent data according to established methods,[22,43] we extract the Stokes parameters (ΔS_{1-3}) and compare them with theoretical inputs. As illustrated in Fig. 4c, the measured parameters show excellent agreement with the expected values. The corresponding detection errors under 300 μW cm^{-2} illumination are ΔS_1 = 1.3%, ΔS_2 = 2.6%, and ΔS_3 = 2.5% (Fig. 4d). This performance significantly surpasses that of a recently reported polarimeter utilizing an analogous (*R*-NEA)PbI_3 polycrystalline thin film (see comparison in Table S1).[19,21] We attribute this enhancement to the pronounced BPVE present in single-crystal devices. Notably, at a low-light intensity of 0.4 μW cm^{-2}, the polarimeter still achieves high accuracy with detection errors of ΔS_1 = 2.0%, ΔS_2 = 3.1%, and ΔS_3 = 3.6% (Fig. S10), enabling full-Stokes polarization detection under ultra-weak illumination conditions that are challenging for conventional optical-filter-based systems. Furthermore, the device shows outstanding long-term stability; its detection accuracy is maintained after 120 days of storage under ambient conditions, with errors for S_{1-3} remaining below 4% (Fig. S11a–c).

To demonstrate practical applications, we perform full-Stokes imaging using a patterned "N" mask illuminated with a known SoP (Fig. 4e). By spatially resolving the Stokes parameters across a 20 × 20 pixel array, we reconstruct high-resolution images corresponding to S_1, S_2, and S_3 (Fig. 4f–h), each exhibiting uniform intensity distribution and clear edge definition. The average detection errors across the array are ΔS_1 = 5.2%, ΔS_2 = 5.9%, and ΔS_3 = 7.1%, confirming the system's reliability in pixel-level polarization imaging. Furthermore, from the pixel-wise Stokes data, we extract the Degree of Linear Polarization (DOLP = $\sqrt{(S_1^2 + S_2^2)}/S_0$) and Degree of Circular

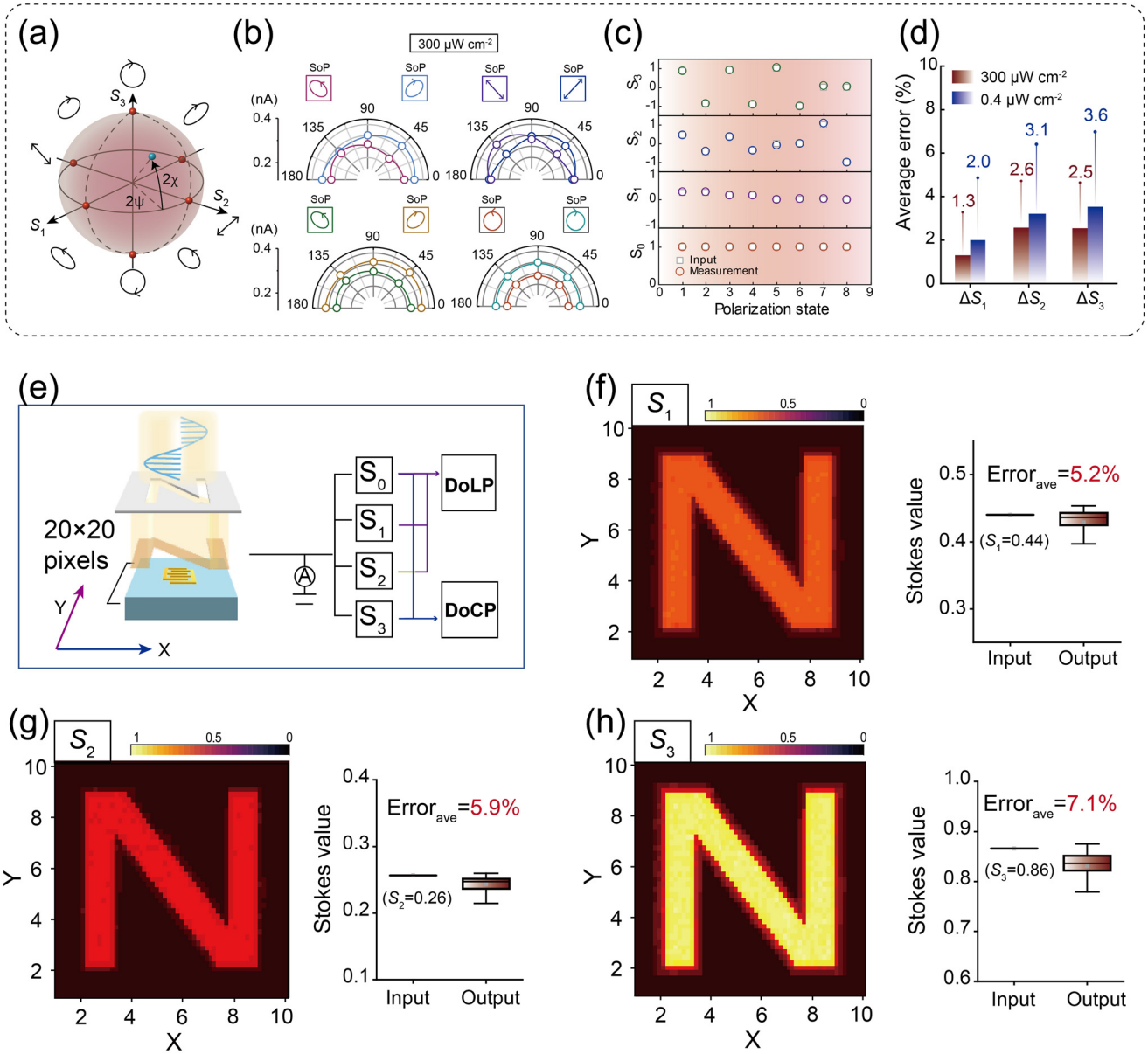

Fig. 4 (a) Poincaré sphere showing representative SoPs. (b) Measured photocurrent of the (*R*-NEA)PbI_3 polarimeter under eight distinct input polarization states, recorded with the rotation stage set to 0°, 45°, 90°, 135°, and 180°; the incident wavelength is 396 nm with an illumination intensity of 300 μW cm^{-2}. (c) Detection errors for the Stokes parameters (S_0–S_3) extracted from the eight input SoPs. (d) Average detection errors for the S_1–S_3 parameters. (e) Schematic illustration of the full-Stokes imaging test: the procedure involved transmitting modulated SoPs through an N-shaped pattern, followed by a step-by-step process to generate a 20 × 20 pixel image array. (f–h) Full-Stokes imaging results for the S_1–S_3 parameters and their corresponding average detection errors.

Polarization (DOCP = $|S_3|/S_0$), yielding DOLP = 0.74 and DOCP = 0.67 from the image recording. This ability to simultaneously capture both linear and circular polarization components demonstrates the polarimeter's robustness for real-time polarization imaging. Notably, unlike conventional division-of-focal-plane polarimeters which require complex optical splitting and at least four detectors per pixel, our filter-less polarimeter offers a compact, monolithic design. This highlights its potential for next-generation in-chip, high-resolution, and energy-efficient full-Stokes imaging systems.

Conclusions

In summary, we developed a high-performance, self-powered full-Stokes polarimeter based on the chiral polar 1D perovskite (*R*/*S*-NEA)PbI_3 SC. The intrinsic BPVE enables efficient photocarrier extraction under zero bias, effectively minimizing the influence of noise currents. As a result, the polarimeter achieves a high D^* of 4.1 × 10^{13} Jones. The strong linear and circular dichroism endows the polarimeter with excellent sensitivity to both LPL and CPL, with a ω of 1.99 and a g_{cpl} of

0.57. These characteristics enable accurate full-Stokes polarization detection, achieving an average error in the Stokes parameters (ΔS_{1-3}) of less than 3%. Remarkably, the polarimeter maintains detection errors below 4% even at an ultra-low light intensity of 0.4 μW cm^{-2}, surpassing the lowest detectable power reported for comparable polarimeters. Furthermore, we demonstrate full-Stokes imaging with clearly resolved S_{1-3} parameter extraction across the image matrix, enabling precise and uniform polarization-resolved imaging.

Experimental section

Materials

Lead(II) oxide (PbO, 99.9%), hydroiodic acid solution (HI, 57% wt/wt), hydrochloric acid solution (H_3PO_4, 37% wt/wt), and *R*-(+)- or *S*-(−)-1-(1-naphthyl)ethylamine were purchased from Aladdin (Shanghai, China).

Syntheses

The prescribed stoichiometric quantities of (*R* or *S*)-NEA (3 mmol), $Pb(Ac)_2{\cdot}3H_2O$ (3 mmol) and hydriodic acid (48 wt%, 12 ml) were used in the experiment. First, 3 mmol of $Pb(Ac)_2{\cdot}3H_2O$ was dissolved in 12 mL of hydriodic acid under continuous stirring. The mixture was gradually heated to 373 K and maintained at this temperature until the solution became completely clear (approximately 10 minutes). Next, 3 mmol of (*R* or *S*)-NEA was added to the clear solution, which was then stirred and heated continuously for an additional 15 minutes. After full dissolution, the solution was slowly cooled to room temperature at a rate of 2 K per hour. Orange-colored rod-like crystals of (*R* or *S*)-$NEAPbI_3$ were obtained upon completion of the cooling process.

Device fabrication

Planar structured photoconductive detectors were fabricated by thermally evaporating Au electrodes onto single crystals, and the channel between neighboring electrodes had a width of 0.5 mm, with lengths of 50, 70, 100, 130, and 180 μm.

Author contributions

Quanlin Chen: writing – original draft, methodology, experiment, and data curation. Yangbin Xu: experiment. Qingming Wu: experiment. Yanxing Feng: review and editing. Zhiqiang Huang: review and editing. Hai Jia: review and editing. Shaoming Ying: supervision, conceptualization and formal analysis – review & editing. Xiaohui Huang: supervision, conceptualization and formal analysis – review & editing.

Conflicts of interest

There are no conflicts to declare.

Data availability

The data supporting this article have been included as part of the supplementary information (SI). Supplementary information: experimental and characterization details including XRD, UV-Vis absorption spectra, CD spectra, Raman spectra and POM image recording. The details of photoelectric studies and polarimetric measurements. See DOI: **https://doi.org/10.1039/d5qi01944c**.

Acknowledgements

Q. Chen acknowledges financial support from the Research Projects of Ningde Normal University (Grant No. 2024Y10), the Foundation for Cultivated Young Talents of Fujian Province, China (Grant No. 2025350147), and the Young and Middle-aged Teacher Education Research Project of Fujian Province of China (Grant No. JAT241161). This work was also supported by the Natural Science Foundation of Fujian Province of China (Grant No. 2024J08226 and 2023J05203) and the Project of Scientific Research of Ningde Normal University (Grant No. 2024ZX01, 2024T02, and 2023Y09).

References

1 M. Ge, Y. Yao, T. Wang, S. Mukherjee, H. Ade and M. Liu, Accurate Single-Shot Full-Stokes Detection Enabled by Heterogeneous Grain Orientations in Polycrystalline Films, *Nat. Commun.*, 2025, **16**, 5603, DOI: **10.1038/s41467-025-60914-y**.

2 G. Myhre, W.-L. Hsu, A. Peinado, C. LaCasse, N. Brock, R. A. Chipman and S. Pau, Liquid Crystal Polymer Full-Stokes Division of Focal Plane Polarimeter, *Opt. Express*, 2012, **20**, 27393–27409, DOI: **10.1364/oe.20.027393**.

3 M. Dai, C. Wang, B. Qiang, F. Wang, M. Ye, S. Han, Y. Luo and Q. J. Wang, On-Chip Mid-Infrared Photothermoelectric Detectors for Full-Stokes Detection, *Nat. Commun.*, 2022, **13**, 4560, DOI: **10.1038/s41467-022-32309-w**.

4 L. Liu, F. Cao, L. Bian, M. Wang, H. Sun and L. Li, Ascorbic Acid-Induced Porous Iodide Layer for a High-Purity Two-Step Solution-Processed Tin-Lead Mixed Perovskite Photodetector, *J. Mater. Sci. Technol.*, 2025, **210**, 227–232, DOI: **10.1016/j.jmst.2024.05.043**.

5 L. Wang, W. Hao, B. Peng, J. Ren and H. Li, Nucleation–Controlled Crystallization of Chiral 2D Perovskite Single Crystal Thin Films for High–Sensitivity Circularly Polarized Light Detection, *Adv. Mater.*, 2025, **37**, 2414199, DOI: **10.1002/adma.202414199**.

6 J. Son, S. Ma, Y.-K. Jung, J. Tan, G. Jang, H. Lee, C. U. Lee, J. Lee, S. Moon, W. Jeong, A. Walsh and J. Moon, Unraveling Chirality Transfer Mechanism by Structural Isomer-Derived Hydrogen Bonding Interaction in 2D Chiral Perovskite, *Nat. Commun.*, 2023, **14**, 3124, DOI: **10.1038/s41467-023-38927-2**.

7 H. Chen, G. Wang, Y. Wang, X. Zhao, X. Xu, L. Zhang, W. Wei and L. Shen, Progress in and Outlook on Polarization-Sensitive Perovskite Photodetectors, *J. Mater. Chem. A*, 2025, **13**, 1711–1730, DOI: **10.1039/d4ta07010k**.

8 Z. Lin, X. Yang, J. He, N. Dong and B. Li, Structural and Optoelectronic Characterization of Anisotropic Two-Dimensional Materials and Applications in Polarization-Sensitive Photodetectors, *Appl. Phys. Rev.*, 2025, **12**, 011301, DOI: **10.1063/5.0226193**.

9 L. Yu, H. Dong, W. Zhang, Z. Zheng, Y. Liang and J. Yao, Development and Challenges of Polarization-Sensitive Photodetectors Based on 2D Materials, *Nanoscale Horiz.*, 2025, **10**, 847–872, DOI: **10.1039/d4nh00624k**.

10 N. A. Rubin, G. D'Aversa, P. Chevalier, Z. Shi, W.-T. Chen and F. Capasso, Matrix Fourier Optics Enables a Compact Full-Stokes Polarization Camera, *Science*, 2019, **365**, eaax1839, DOI: **10.1126/science.aax1839**.

11 M. K. Jana, R. Song, Y. Xie, R. Zhao, P. C. Sercel, V. Blum and D. B. Mitzi, Structural Descriptor for Enhanced Spin-Splitting in 2D Hybrid Perovskites, *Nat. Commun.*, 2021, **12**, 4982, DOI: **10.1038/s41467-021-25149-7**.

12 A. Ishii, R. Sone, T. Yamada, M. Noto, H. Suzuki, D. Nakamura, K. Murata, T. Shiga, K. Ishii and M. Nihei, Giant Bulk Photovoltaic Effect in a Chiral Polar Crystal Based on Helical One–Dimensional Lead Halide Perovskites, *Angew. Chem., Int. Ed.*, 2025, **64**, e202424391, DOI: **10.1002/ange.202424391**.

13 H. Wu, Z. Xu, X. Dong, L. Wang, J. Liang, T. Chen, X. Li, L. Li and J. Luo, Precise Design of Chiral-Polar Hybrid Perovskites toward Efficient Self-Powered Full-Stokes Photodetection, *Innovation Mater.*, 2024, **2**, 100084, DOI: **10.59717/j.xinn-mater.2024.100084**.

14 Y. Zhao, Y. Qiu, J. Feng, J. Zhao, G. Chen, H. Gao, Y. Zhao, L. Jiang and Y. Wu, Chiral 2D-Perovskite Nanowires for Stokes Photodetectors, *J. Am. Chem. Soc.*, 2021, **143**, 8437–8445, DOI: **10.1021/jacs.1c02675**.

15 Z. Xu, T. Chen, J. Liang, X. Dong, Y. Geng, L. Li, Z. Sun and J. Luo, Achieving Efficient Self–Driven Full–Stokes Photodetection in Optically Active Ferroelectric, *Angew. Chem., Int. Ed.*, 2025, **64**, e202513386, DOI: **10.1002/anie.202513386**.

16 Q. Liu, P. Wang, Q. Wei, L. Zhou, H. Ren, C. Wang, J. Peng, L. Zhao and M. Li, Chiral Perovskite Nanowire Optoelectronic Synapse for Full–Stokes Polarization–Resolved Perception and Reservoir Computing, *Adv. Funct. Mater.*, 2025, **35**, 2415551, DOI: **10.1002/adfm.202415551**.

17 Y. Zhao, Z. Zhou, X. Liu, A. Ren, S. Ji, Y. Guan, Z. Liu, H. Liu, P. Li, F. Hu and Y. S. Zhao, Chiral 2D/Quasi–2D Perovskite Heterojunction Nanowire Arrays for High–Performance Full–Stokes Polarization Detection, *Adv. Opt. Mater.*, 2023, **11**, 2301239.

18 J. Bai, H. Wang, J. Ma, Y. Zhao, H. Lu, Y. Zhang, S. Gull, T. Qiao, W. Qin, Y. Chen, L. Jiang, G. Long and Y. Wu, Wafer-Scale Patterning Integration of Chiral 3D Perovskite Single Crystals toward High-Performance Full-Stokes Polarimeter, *J. Am. Chem. Soc.*, 2024, **146**, 18771–18780, DOI: **10.1021/jacs.4c06822**.

19 C. Wang, G. Li, Z. Dai, W. Tian and L. Li, Patterned Chiral Perovskite Film for Self–Driven Stokes Photodetectors, *Adv. Funct. Mater.*, 2024, **34**, 2316265, DOI: **10.1002/adfm.202316265**.

20 Q. Chen, M. Ge, C. Geng, J. Zhang, L. Gao, Z. Huang, S. Wang, Y. Feng, X. Yue, S. M. H. Qaid, X. Fu, M. Wang, Y. Jiang and M. Yuan, Manipulating Perovskite Structural Asymmetry for High-Performing Self-Powered Full-Stokes Polarimetry, *Sci. Adv.*, 2025, **11**, eads6123, DOI: **10.1126/sciadv.ads6123**.

21 Q. Chen, Z. Ding, L. Zhang, D. Wang, C. Geng, Y. Feng, J. Zhang, M. Ren, S. Li, Q. Saif, Y. Jiang and M. Yuan, Uniaxial–Oriented Chiral Perovskite for Flexible Full–Stokes Polarimeter, *Adv. Mater.*, 2024, **36**, 2400493.

22 J. Ma, F. Chen, L. Liang, H. Wang and D. Li, Full–Stokes Polarimeter Based on Chiral Perovskites with Chirality and Large Optical Anisotropy, *Small*, 2021, **17**, 2103855, DOI: **10.1002/smll.202103855**.

23 H. Ye, Y. Peng, M. Wei, X. Zhang, T. Zhu, Q. Guan, L. Li, S. Chen, X. Liu and J. Luo, Bulk Photovoltaic Effect in Chiral Layered Hybrid Perovskite Enables Highly Sensitive Near-Infrared Circular Polarization Photodetection, *Chem. Mater.*, 2023, **35**, 6591–6597, DOI: **10.1021/acs.chemmater.2c03770**.

24 S. Han, M. Li, Y. Liu, W. Guo, M.-C. Hong, Z. Sun and J. Luo, Tailoring of a Visible-Light-Absorbing Biaxial Ferroelectric towards Broadband Self-Driven Photodetection, *Nat. Commun.*, 2021, **12**, 284, DOI: **10.1038/s41467-020-20530-4**.

25 T. Wang, K. Zhao, P. Wang, W. Shen, H. Gao, Z. Qin, Y. Wang, C. Li, H. Deng, C. Hu, L. Jiang, H. Dong, Z. Wei, L. Li and W. Hu, Intrinsic Linear Dichroism of Organic Single Crystals toward High–Performance Polarization–Sensitive Photodetectors, *Adv. Mater.*, 2021, **34**, 2105665, DOI: **10.1002/adma.202105665**.

26 Z. Zhang, Z. Wang, H. H.-Y. Sung, I. D. Williams, Z.-G. Yu and H. Lu, Revealing the Intrinsic Chiroptical Activity in Chiral Metal-Halide Semiconductors, *J. Am. Chem. Soc.*, 2022, **144**, 22242–22250, DOI: **10.1021/jacs.2c10309**.

27 C. Zhang, Z. Wu, W. Zhang, Q. Guan, H. Ye, R. Li, H. Li, Z.-K. Zhu, P. Wang, Y. Wang, Y. Fang and J. Luo, Chiral-Polar Photovoltage-Driven Efficient Self-Powered Circularly Polarized Light Detection in Three-Dimensional Hybrid Perovskites, *J. Am. Chem. Soc.*, 2025, **147**, 9686–9693, DOI: **10.1021/jacs.4c17796**.

28 Q. Guan, T. Zhu, Z. Zhu, H. Ye, S. You, P. Xu, J. Wu, X. Niu, C. Zhang, X. Liu and J. Luo, Unprecedented Chiral Three–Dimensional Hybrid Organic–Inorganic Perovskitoids, *Angew. Chem., Int. Ed.*, 2023, **62**, e202307034, DOI: **10.1002/anie.202307034**.

29 S. Sun, J. Jiang, M. Jia, Y. Tian and Y. Xiao, 1.5D Chiral Perovskites Mediated by Hydrogen–Bonding Network with Remarkable Spin–Polarized Property, *Angew. Chem., Int. Ed.*, 2025, **64**, e202423314, DOI: **10.1002/anie.202423314**.

30 A. Pietropaolo, A. Mattoni, G. Pica, M. Fortino, G. Schifino and G. Grancini, Rationalizing the Design and Implementation of Chiral Hybrid Perovskites, *Chem*, 2022, **8**, 1231–1253, DOI: **10.1016/j.chempr.2022.01.014**.

31 A. Ishii and T. Miyasaka, Direct Detection of Circular Polarized Light in Helical 1D Perovskite-Based Photodiode, *Sci. Adv.*, 2020, **6**, eabd3274, DOI: **10.1126/sciadv.abd3274**.

32 S. Y. Yang, J. Seidel, S. J. Byrnes, P. Shafer, C.-H. Yang, M. D. Rossell, P. Yu, Y.-H. Chu, J. F. Scott, J. W. Ager, L. W. Martin and R. Ramesh, Above-Bandgap Voltages from Ferroelectric Photovoltaic Devices, *Nat. Nanotechnol.*, 2010, **5**, 143–147, DOI: **10.1038/nnano.2009.451**.

33 C. Ji, Y. Li, X. Liu, Y. Wang, T. Zhu, Q. Chen, L. Li, S. Wang and J. Luo, Monolayer–To–Multilayer Dimensionality Reconstruction in a Hybrid Perovskite for Exploring the Bulk Photovoltaic Effect Enables Passive X–Ray Detection, *Angew. Chem., Int. Ed.*, 2021, **60**, 20970–20976, DOI: **10.1002/anie.202108145**.

34 C. Ji, D. Dey, Y. Peng, X. Liu, L. Li and J. Luo, Ferroelectricity–Driven Self–Powered Ultraviolet Photodetection with Strong Polarization Sensitivity in a Two–Dimensional Halide Hybrid Perovskite, *Angew. Chem., Int. Ed.*, 2020, **59**, 18933–18937, DOI: **10.1002/anie.202005092**.

35 Z. Li, C. Ji, Y. Fan, T. Zhu, S. You, J. Wu, R. Li, Z.-K. Zhu, P. Yu, X. Kuang and J. Luo, Circularly Polarized Light-Dependent Pyro-Phototronic Effect from 2D Chiral–Polar Double Perovskites, *J. Am. Chem. Soc.*, 2023, **145**, 25134–25142, DOI: **10.1021/jacs.3c05080**.

36 Q. Chen, Z. Huang, X. Liao, M. Ren, X. Huang and S. Ying, Chiral Bismuth Halide Crystals: Polarizability-Driven Birefringence and Wave Plate Functionality, *Inorg. Chem.*, 2025, **64**(42), 21177–21184.

37 S. Chen, J. Wang, G. Ran, Q. Pan, L. Liu, C. Zhao, J. Tang, M. Zhao, W. Zhang, Y. Zhao and T. Jiu, Control of the Surface Disorder by Ion–Exchange to Achieve High Open–Circuit Voltage in $HC(NH_2)_2PbI_3$ Perovskite Solar Cell, *Small Methods*, 2021, **5**, 2101079, DOI: **10.1002/smtd.202101079**.

38 S. Chen, Q. Pan, J. Li, C. Zhao, X. Guo, Y. Zhao and T. Jiu, Grain Boundary Passivation with Triazine-Graphdiyne to Improve Perovskite Solar Cell Performance, *Sci. China Mater.*, 2020, **63**, 2465–2476, DOI: **10.1007/s40843-020-1324-8**.

39 Q. Chen, J. Zhang, L. Zhang, Y. Feng, D. Wang, Z. Ding, C. Geng, S. M. H. Saif, Y. Jiang and M. Yuan, Efficient Charge Injection for Perovskite Light–Emitting Transistor, *Adv. Opt. Mater.*, 2024, **12**, 2400447, DOI: **10.1002/adom.202400447**.

40 F. Chen, J. Li, B. Zhou and D. Li, Self-Powered Filterless On-Chip Full-Stokes Polarimeter, *Nano Lett.*, 2021, **21**, 6156–6162, DOI: **10.1021/acs.nanolett.1c01729**.

41 J. Wang, C. Jiang, W. Li and X. Xiao, Anisotropic Low–Dimensional Materials for Polarization–Sensitive Photodetectors: From Materials to Devices, *Adv. Opt. Mater.*, 2022, **10**, 2102436, DOI: **10.1002/adom.202102436**.

42 X. Wang, Y. Wang, W. Gao, L. Song, Z. Wu, Y. Chen and W. Huang, Polarization–Sensitive Halide Perovskites for Polarized Luminescence and Detection: Recent Advances and Perspectives, *Adv. Mater.*, 2021, **33**, 2003615, DOI: **10.1002/adma.202003615**.

43 W. Zhang, M. Hong and J. Luo, Centimeter-Sized Single Crystal of a One-Dimensional Lead-Free Mixed-Cation Perovskite Ferroelectric for Highly Polarization Sensitive Photodetection, *J. Am. Chem. Soc.*, 2021, **143**, 16758–16767, DOI: **10.1021/jacs.1c08281**.